Nano Research

Open Access

Research Article

Mussel-bionic fiber@ZnO composite membrane for self-cleaning antibacterial mask

Yong Wang[1], Wen-Bo Zhao[1], Fu-Kui Li[1], Shulong Chang[1], Bao-Shuai Shi[1], Lin Jia[1], Kai-Kai Liu[1,2] ✉, and Chong-Xin Shan[1] ✉

[1] *Henan Key Laboratory of Diamond Optoelectronic Materials and Devices, Key Laboratory of Material Physics, Ministry of Education, School of Physics, Zhengzhou University, Zhengzhou 450052, China*
[2] *Institute of Quantum Materials and Physics Henan Academy of Sciences, Zhengzhou 450046, China*

Cite this article: *Nano Research*, **2025**, *18*, 94907205. https://doi.org/10.26599/NR.2025.94907205

ABSTRACT: The COVID-19 pandemic has underscored the significance of antibacterial protective materials. Utilizing high-performance antibacterial masks proves to be effective in preventing the spread of respiratory diseases. Herein, we demonstrate a self-cleaning antibacterial mask constructed from the fiber@ZnO composite membrane, utilizing the strong interfacial adhesion of polydopamine (PDA). With a ZnO NPs immersion solution concentration of 1.0 mg/mL, the ZnO NP content in fiber@ZnO reaches 6.5%. The fiber@ZnO demonstrates bactericidal rates exceeding 99% against Gram-positive (*S. aureus*) and Gram-negative (*E. coli*) bacteria, and exhibits an inhibition rate exceeding 99.99% against the H1N1 influenza virus. The hydrogen bonding and electrostatic interaction between ZnO nanoparticles (NPs) and PDA can keep a stable combination of NPs and fiber. Antibacterial masks constructed by the fiber@ZnO composite membrane exhibit superior self-cleaning performance and effectively eliminate pathogenic bacteria in aerosols compared with commercial N95 masks. The mussel-bionic strategy presents a viable approach for developing novel antibacterial fibers, with significant application potential in reducing the risk of human infection and preventing the re-transmission of pathogens.

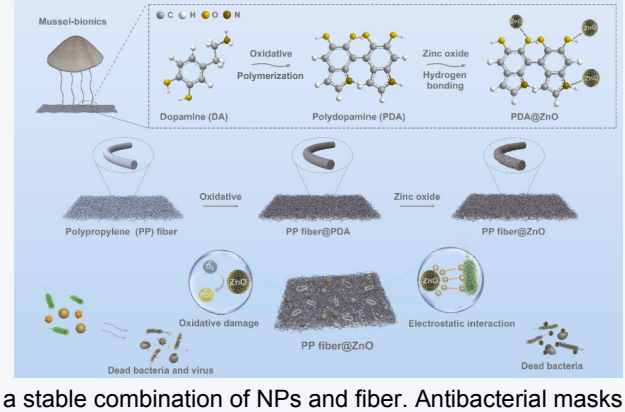

KEYWORDS: antibacterial mask, biomimetics, fiber, ZnO, nanoparticles

1 Introduction

Infectious diseases, caused by harmful bacteria and viruses, pose a serious threat to the health and safety of human beings. A prominent example is the COVID-19 pandemic that began in 2019, resulting in tens of thousands of confirmed and fatal cases within just a few years. This has had profound impacts on human health, as well as on social and economic development [1–3]. COVID-19 is just one of the many pathogenic diseases that pose a threat to public health, with respiratory diseases like influenza and pneumonia ever-present in people's lives [4, 5]. Respiratory transmission is an important route for bacteria, mycoplasma, viruses, and other pathogens to infect humans. Therefore, wearing personal protective equipment is an effective method to reduce damage to the human body from harmful gases, droplets, viruses, and other substances [6, 7]. As a simple and cost-effective method, wearing a mask can effectively limit the spread of disease. However, it cannot eliminate the risk of infection, as the mask can only partially trap pathogens on the surface of the filter layer and cannot inactivate the intercepted microorganisms [8, 9]. Ultimately, the filter layer can easily become a breeding ground for pathogenic microorganisms. When pathogens accumulate on the mask, the protective effect will be compromised, and prolonged or repeated use of disposable masks will increase the wearer's infection risk. In addition, improper disposal of discarded masks can cause cross-contamination and increase the risk of secondary transmission of pathogens [10, 11]. Therefore, developing new antibacterial mask filter materials plays a crucial role in reducing the risk of infection and mitigating waste pollution.

To enhance the protective performance of masks, the most extensively researched methods currently include improving the

Received: October 14, 2024; **Revised:** December 12, 2024
Accepted: December 19, 2024

✉Address correspondence to Kai-Kai Liu, liukaikai@zzu.edu.cn; Chong-Xin Shan, cxshan@zzu.edu.cn

filtration performance and antibacterial activity of fiber membranes through plasma treatment, surface modification, melt blending, electrospinning, post-finishing, and genetic engineering technology [12–18]. Electrospinning technology is used to produce nanofibers to enhance the filtration efficiency of the fiber membrane against microorganisms [14]. The surface polarity of the fiber is strengthened through chemical surface modification, and further improving filtration effectiveness [13]. Additionally, the retention time of static charge on the surface of the filter layer can enhance filtration performance and extend the life of the mask [17]. While these methods can enhance protection safety by improving filtration performance, it should be noted that microorganisms remaining in the filter layer still pose a certain risk of infection to humans. In contrast, while ensuring filtration performance, it is particularly important to enhance the protective safety of masks by endowing the filter layer with the ability to inactivate microorganisms [12]. To impart antibacterial properties to the filter layer, fibers are commonly combined with various antibacterial agents, such as plant extracts, chitosan, halides, quaternary ammonium compounds, metal-organic frameworks, metal nanoparticles, metal oxides, and so on [19–21]. However, the antibacterial activity of modified fiber membranes is commonly influenced by the stability of the bactericide, irreversible consumption, the requirement for external stimulation to function, and biological safety. Simultaneously, these methods are also associated with drawbacks like high costs, complex preparation processes, and inability to be widely used in industry [21]. Therefore, it is crucial to provide the filter layer with spontaneous and sustained antibacterial activity through a simple and economical method.

Polypropylene (PP) fibers are extensively used in industry as the filter layer of masks, playing a crucial role in adsorption filtration, medical, and healthcare applications owing to their straightforward production process, cost-effectiveness, and favorable physical and mechanical properties [22]. Hence, it is of great practical significance to enable commercial PP fibers to have spontaneous and sustained antibacterial properties. However, due to the single molecular structure of PP and the lack of polar functional groups on the surface, the interface adhesion between antibacterial agents and PP fibers is weak, which limits its application scope to a certain extent [23, 24]. Achieving an effective combination of antibacterial agents and PP fibers has become a key issue in preparing efficient antibacterial PP fibers. In recent years, mussel-inspired chemistry has attracted considerable attention for its excellent adhesive properties [25–27]. Dopamine is widely recognized as the most commonly used mussel-inspired compound. It can auto-oxidize and polymerize in alkaline aqueous solutions to form polydopamine (PDA) coatings with robust adhesion. PDA is rich in catechol and amine functional groups, allowing it to adhere to nearly all types of surfaces through covalent bonds or non-covalent bonds, without the need for surface pretreatment. The reaction conditions are mild and do not damage the substrate, providing a simple and versatile method to functionalize material surfaces [28, 29]. The robust interfacial adhesion of PDA was used to modify the surface of PP fiber, providing the possibility for an effective combination of the antibacterial agent with PP fiber.

In this work, a fiber@ZnO composite membrane with antibacterial properties was fabricated using biomimetic surface modification strategies inspired by the adhesion mechanism of mussels. The PDA film was formed on the surface of commercial PP fibers through the autoxidative polymerization and self-assembly process of dopamine. Subsequently, ZnO nanoparticles (NPs) were deposited onto the PP fibers through hydrogen bonding interaction and electrostatic interaction between the NPs and PDA, and the robust interfacial adhesion of PDA facilitated the stable attachment of NPs to PP fibers. The electrostatic interactions between NPs and bacteria, along with the disruption of bacterial cell membranes and the proteins and nucleic acids of viruses by reactive oxide species (ROS), resulted in the spontaneous and sustained broad-spectrum antibacterial and antiviral activity of the fiber@ZnO composite membrane. Compared with commercial N95 masks, antibacterial masks constructed by the fiber@ZnO composite membrane can autonomously and continuously kill bacteria in aerosols without requiring external stimulation, the bactericidal rates exceeding 99% against both Gram-positive (*S. aureus*) and Gram-negative (*E. coli*) bacteria, and exhibits an inhibition rate exceeding 99.99% against the H1N1 influenza virus, demonstrating superior self-cleaning performance. This study demonstrates the feasibility of integrating commercial PP fibers with ZnO NPs as a mask filtration layer with durable and spontaneous antibacterial activity. This innovation holds significant potential for application in reducing the risk of human infections and preventing the re-transmission of pathogens, presenting a promising prospect in the market.

2 Experimental

2.1 Materials

Zinc acetate dihydrate ($Zn(Ac)_2{\cdot}2H_2O$), potassium hydroxide (KOH), dopamine hydrochloride (98%), tris-hydrochloride buffer (1 M, pH = 8.5), phosphate buffered (PBS) and glutaraldehyde were obtained from Aladdin Chemistry Co., Ltd. (Shanghai, China). Absolute ethanol was purchased from Tianjin Yongda Chemical Reagent Co., Ltd. (Tianjin, China). Commercial polypropylene fiber was purchased from Cofoe Medical Technology Co., Ltd. (Hunan, China). The commercial N95 mask was purchased from Henan Yubei Sanitary MATERIALS Co., Ltd. (Henan, China). Aerosol generator was purchased from Qingdao SuYuan Environmental Protection Equipment Co, Ltd. (Shandong, China). LIVE/DEAD BacLight bacterial viability kit (L13152) was purchased from Invitrogen Corporation (USA). Deionized water used in all experiments was obtained by purifying water with a Millipore system using a Waterjet laboratory dedicated ultrapure water machine. All chemicals were reagents above analytical grade and were not further purified when used.

2.2 Synthesis of ZnO NPs

ZnO NPs were synthesized by a modified sol–gel route. In brief, 16.62 g of $Zn(Ac)_2{\cdot}2H_2O$ was dissolved in 300 mL ethanol solution and stirred for 0.5 h at room temperature, continuously. Meanwhile, 6.18 g of KOH was dissolved in 150 mL of ethanol solution, and the mixture was stirred for 0.5 h until KOH was completely dissolved. Subsequently, the KOH solution was added to the $Zn(Ac)_2{\cdot}2H_2O$ ethanol solution and stirred for 2 h. Finally, the ZnO solution is formed.

2.3 Preparation of fiber@ZnO composite membrane

At first, the PP fiber membrane was cleaned with deionized water and ethanol to remove impurities and dried for further processing.

Then, the PP fiber membrane was immersed in a dopamine hydrochloride solution (2 mg/mL in 10 mM of tris-hydrochloride buffer, pH 8.5) at room temperature. After slight stirring for 24 h, the PDA-coated PP fiber was washed with deionized water and dried for 1 h to obtain the fiber@PDA fiber membrane. After that, the fiber@PDA fiber membrane was immersed in different concentrations of ZnO NPs solutions (0.1, 0.5, and 1.0 mg/mL) at room temperature for 2 h. Finally, the fiber@ZnO composite membranes were obtained after drying for 1 h, which were named fiber@ZnO-0.1, fiber@ZnO-0.5, and fiber@ZnO-1.0 based on the concentration of ZnO solution. And, it is worth noting that the fiber@ZnO in the manuscript is fiber@ZnO-1.0.

2.4 Characterization

The size and morphology of ZnO NPs were characterized by Transmission electron microscopy (TEM) on an HT7700 from Hitachi, Japan. The crystal structure of the samples was detected by X-ray diffraction (XRD) using a D8 Discover instrument from Bruker, Germany. The fluorescence spectra of ZnO NPs were measured on an FLS 1000 spectrometer. The Fourier transform infrared spectra (FTIR) of the samples were characterized by an FTIR spectrometer (Nicolet 6700, Thermo Fisher Scientific, USA). The zeta potential of ZnO NPs and bacteria was detected by a Zeta-sizer Nano Particle Analyzer (ZEN5600, Malvern, UK). The chemical composition of the samples was characterized by X-ray photoelectron spectroscopy (XPS, EscaLab 250Xi, Thermo Fisher Scientific, USA). The surface morphology of the fiber membrane and bacteria was characterized by field-emission scanning electron microscopy (SEM, JSM-6700F, JEOL, Japan). The pore size of the fibers was measured through indentation testing (Micromeritics 9620, USA). The water contact angle of fibers was measured by a contact angle goniometer (Dataphysics OCA20, Germany). The mechanical properties of the fiber membrane were determined using a single-column tester (Instron 5943). The air permeability of the fiber membrane was determined by the YG461E fabric breathable performance tester.

2.5 Antibacterial and antiviral activity of the fiber@ZnO composite membrane

2.5.1 Antibacterial activity of the fiber@ZnO composite membrane

S. aureus and *E. coli* were selected as representatives of Gram-positive and Gram-negative bacteria to evaluate the antibacterial activity of the fiber@ZnO composite membrane in this work. Briefly, a single colony of each bacterial strain was respectively incubated at 37 °C for 13 h, reaching the exponential phase of bacterial growth (about 10^9 CFU/mL). The antibacterial properties of the pristine PP fibers and fiber@ZnO composite membranes were evaluated according to the plate counting method. Firstly, 0.2 g of the pristine PP fibers or fiber@ZnO composite membranes were placed in 20 mL of the bacterial solution at a concentration of 10^6 CFU/mL, and incubated for 1 h at room temperature. Then, the bacterial suspensions were serially diluted and spread on an Luria-Bertani (LB) agar plate. After incubation at 37 °C for 24 h, the antibacterial ability of the fiber@ZnO composite membrane was analyzed by the change in the number of bacteria.

2.5.2 Antiviral activity of the ZnO NPs and fiber@ZnO composite membrane

The inhibitory activity of ZnO NPs and fiber@ZnO against Influenza A virus H1N1 was tested by the Microbial Analysis and Testing Center of Guangdong Province, China. The testing of ZnO NPs was conducted in accordance with the *Disinfection Technical Specifications* (2002 edition) Sections 2.1.1.10.6 and 2.1.1.10.7. The testing of fiber@ZnO followed the methods outlined in ISO 18184:2019 (E).

2.5.3 Growth inhibition assay

100 μL of bacterial suspension with a concentration of 10^6 CFU/mL was added into a 20 mL LB medium containing different types of samples (blank control and fiber@ZnO composite membranes). Then, the bacterial suspensions were incubated at 37 °C and 180 rpm for 10 h. Every 1 h, 100 μL of bacterial suspensions were pipetted into 96-well plates, and the optical density (OD) at 600 nm was measured using a Varioskan LUX multimode reader (VLBL00D1, Thermo Fisher).

2.5.4 Antibacterial activity of the fiber@ZnO composite membrane in antibacterial mask

The fiber@ZnO composite membrane was placed between the first layer and the second layer of the N95 mask. *E. coli* and *S. aureus* were used as a representative for bacteria, and *E. coli*-laden aerosols or *S. aureus*-laden aerosols generated with an aerosol generator were used as a model for bacterial-laden aerosols. Firstly, bacteria-laden aerosols with a diameter of 1–5 μm were generated from 10^6 CFU/mL of bacteria suspension. Then, the fiber@ZnO mask was exposed to the aerosol flow for 10 min, followed by incubation at room temperature for 60 min. After that, each layer of the fiber@ZnO mask was fully washed with 10 mL PBS solution, and the number of bacteria in PBS eluent was assessed by the plate count method. At the same time, each layer of the fiber@ZnO mask was washed and incubated in LB agar plates for 24 h at 37 °C for residual analysis of adhered viable bacteria. In addition, the antibacterial performance of commercial N95 masks was assessed under the same conditions described above.

2.6 LIVE/DEAD fluorescence assay

Bacterial viability was assessed using confocal laser scanning microscopy (CLSM) and stained with the LIVE/DEAD BacLight Bacterial Viability Kit. The bacterial suspensions were collected by centrifugation at 5000 rpm for 10 min after treatment with pristine PP or fiber@ZnO. Then, the bacteria were stained with SYTO-9 and propidium iodide (PI) at room temperature for 15 min in the dark. The stained bacteria were washed twice with PBS and observed by confocal laser scanning microscopy with 488/525 nm and 488/630 nm as the excitation/emission wavelengths for green and red fluorescence, respectively.

2.7 Morphological characterization of the bacteria

To investigate the potential disruption of bacterial cell membranes by ZnO NPs, morphological changes in the bacteria were assessed by SEM. After treatment with pristine PP or fiber@ZnO composite membrane, bacterial suspensions were collected by centrifugation at 5000 rpm for 10 min. Subsequently, the bacteria were fixed in 2.5% glutaraldehyde for 24 h at 4 °C. Afterward, the bacteria were washed with sterile water and underwent sequential dehydration using varying concentrations of alcohol (20%, 40%, 60%, 80%, and 100%, each step lasting 20 min). In the end, the bacteria were dried, affixed to a copper column with conductive resin, and sputtered with gold, and the morphology of bacterial cells was observed by SEM.

2.8 Statistical analysis

All the data from the experiments were performed at least three times and the results were presented as means ± SD. All statistical analyses were performed in GraphPad Prism 8. Student's *t*-test or one-way analysis of variance (ANOVA) was performed for statistical analysis. *P* value < 0.05 was considered statistically significant, $p > 0.05$ (non significant), $^{*}p < 0.05$, $^{**}p < 0.01$, and $^{***}p < 0.001$.

3 Results and discussion

3.1 Fabrication and sterilization process of the fiber@ZnO composite membrane

The schematic diagram of the fabrication and sterilization process of the fiber@ZnO composite membrane is illustrated in Fig. 1. Due to the simple molecular structure of PP fibers and the lack of polar functional groups on the surface, the interfacial adhesion between ZnO and PP fibers is weak, making it difficult for ZnO to effectively adhere to the PP fibers [23]. To achieve effective bonding between ZnO and PP fibers, we employed a mussel-inspired adhesion mechanism. Mussels adhere to diverse surfaces using proteins rich in catechol and amine functional groups [27]. Inspired by this natural mechanism, we enhanced the adhesion between PDA and PP fibers by applying a PDA coating. Dopamine, a widely used mussel-inspired compound, undergoes an autoxidative polymerization process to form a PDA coating on the surface of PP fibers [30, 31]. This PDA layer, rich in catechol and amine functional groups, facilitates stable attachment to the PP fiber through non-covalent interactions, including hydrogen bonding and π–π interactions [32]. Once the PDA layer was established (resulting in fiber@PDA), ZnO NPs were stably deposited onto the fiber@PDA fibers via hydrogen bonding between the NPs and the PDA. Meanwhile, ZnO NPs and fiber@PDA possess opposite zeta potentials (Fig. S1 in the Electronic Supplementary Material (ESM)), leading to electrostatic attraction between the PDA film and ZnO, which further facilitates the attachment of ZnO NPs, thereby realizing the fabrication of the fiber@ZnO composite membrane. The electrostatic interactions between ZnO NPs and bacteria, along with the generation of ROS that damage the bacterial cell membrane and the proteins and nucleic acids of viruses, result in the fiber@ZnO composite membrane exhibiting spontaneous and sustained broad-spectrum antibacterial and antiviral activity [33–36]. Thus, antibacterial masks constructed by the fiber@ZnO composite membrane exhibit superior self-cleaning performance and effectively eliminate pathogenic microorganisms in aerosols.

3.2 Synthesis and characterization of the ZnO NPs

ZnO NPs exhibit efficient and stable antibacterial activity [37], which makes it possible for the fiber@ZnO composite membrane to possess excellent broad-spectrum antibacterial properties. The size and structure of ZnO NPs were characterized by TEM, as shown in Fig. S2(a) in the ESM. TEM images depict spherical ZnO NPs with a diameter of approximately 4 nm. The high-resolution TEM (HRTEM) image of the ZnO NPs (inset of Fig. S2(a) in the ESM) reveals distinct lattice fringes with a spacing of about 0.26 nm, corresponding to the inter-planar spacing of the (002) planes in wurtzite ZnO [38]. The FTIR of the ZnO NPs are shown in Fig. S2(b) in the ESM, the peaks appear at 3390 cm^{-1} can be attributed to the stretching vibration mode of O–H, the N–H bending peaks appear at 3230 and 1585 cm^{-1}, the peaks centered at around 451 cm^{-1} corresponding to the stretching vibration of Zn–O [37, 39]. The XRD pattern of the ZnO NPs is shown in Fig. S2(c) in the

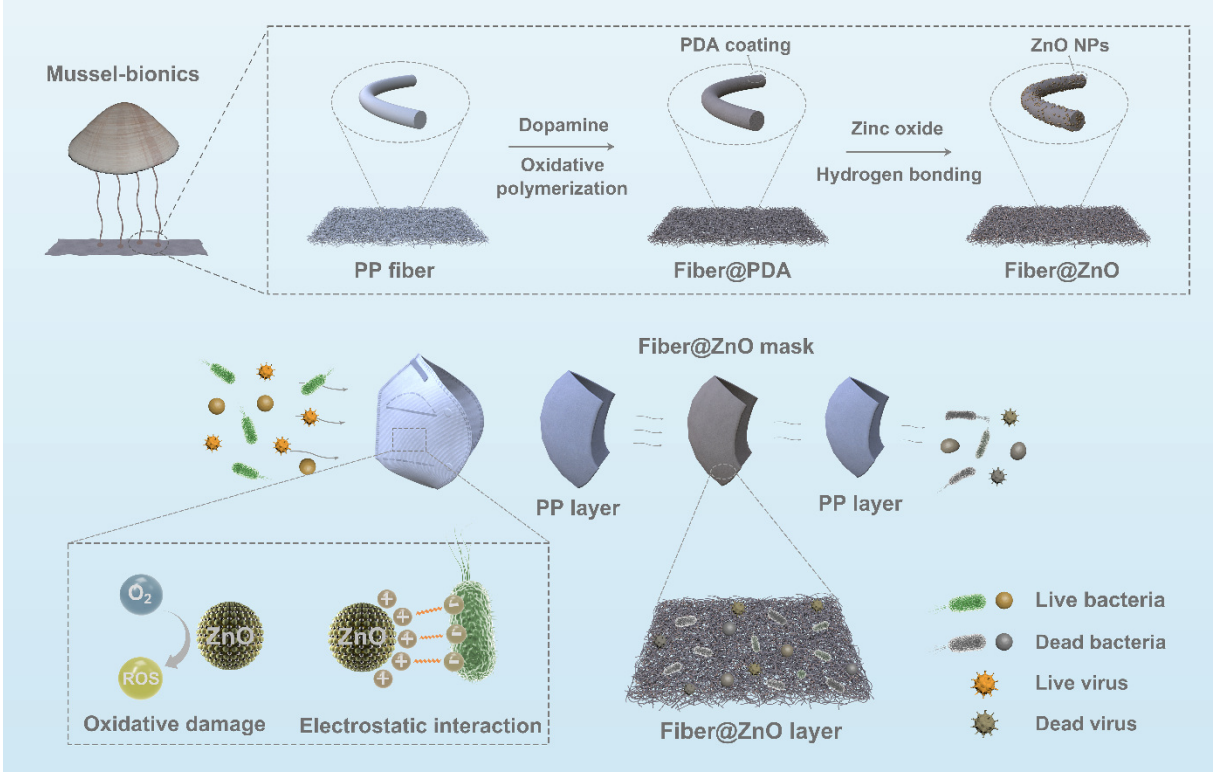

Figure 1 Schematic diagram of the fabrication process (top) and sterilizing process (bottom) of the fiber@ZnO composite membrane.

ESM. It can be observed that the diffraction peaks of (100), (002), (101), (102), (110), (103), and (112) facets attributed to the diffraction from the typical wurtzite ZnO (JCPDS 89-1397) [40]. The excitation spectrum and photoluminescence (PL) spectrum were recorded using the FLS-1000 spectrometer (Fig. S2(d) in the ESM), the excellent luminescence derived from singlet/triplet exciton emission has been verified in our previous work [41], and this can be considered as markers indicating the presence of NPs in the fiber@ZnO composite membrane.

3.3 Preparation and characterization of the fiber@ZnO composite membrane

Due to the color of the PDA solution changing from colorless to brown during the autoxidative polymerization of dopamine, the fiber@ZnO composite membrane exhibits an obvious change under visible light after coating a PDA film, as shown in Fig. 2(a). The optical images of the fiber@ZnO composite membrane under the radiation of 365 nm ultraviolet (UV) light are shown in Fig. S3 in the ESM, emitting a bright yellow color compared to the pristine PP fiber membrane, indicating the successful loading of ZnO NPs onto the fiber@ZnO composite membrane. It can be seen from the SEM images that the surface of the pristine PP fibers is flat and smooth (Figs. 2(b) and 2(c)). After the autoxidative polymerization and self-assembly process of dopamine, the aggregation of PDA particles enhances the roughness of the PP fiber surface, and a relatively homogeneous layer of PDA film is wrapped around the surface of the PP fibers (Fig. S4 in the ESM). As shown in Figs. 2(d) and 2(e), the small size and good dispersion of the ZnO NPs contribute to the minimal alteration of the fiber morphology upon the attachment of NPs to PP fibers. The N and Zn elements in the energy dispersive spectrometer (EDS) image indicate the presence of the PDA coating and the successful adhesion of NPs (Fig. 2(f) and Fig. S5 in the ESM).

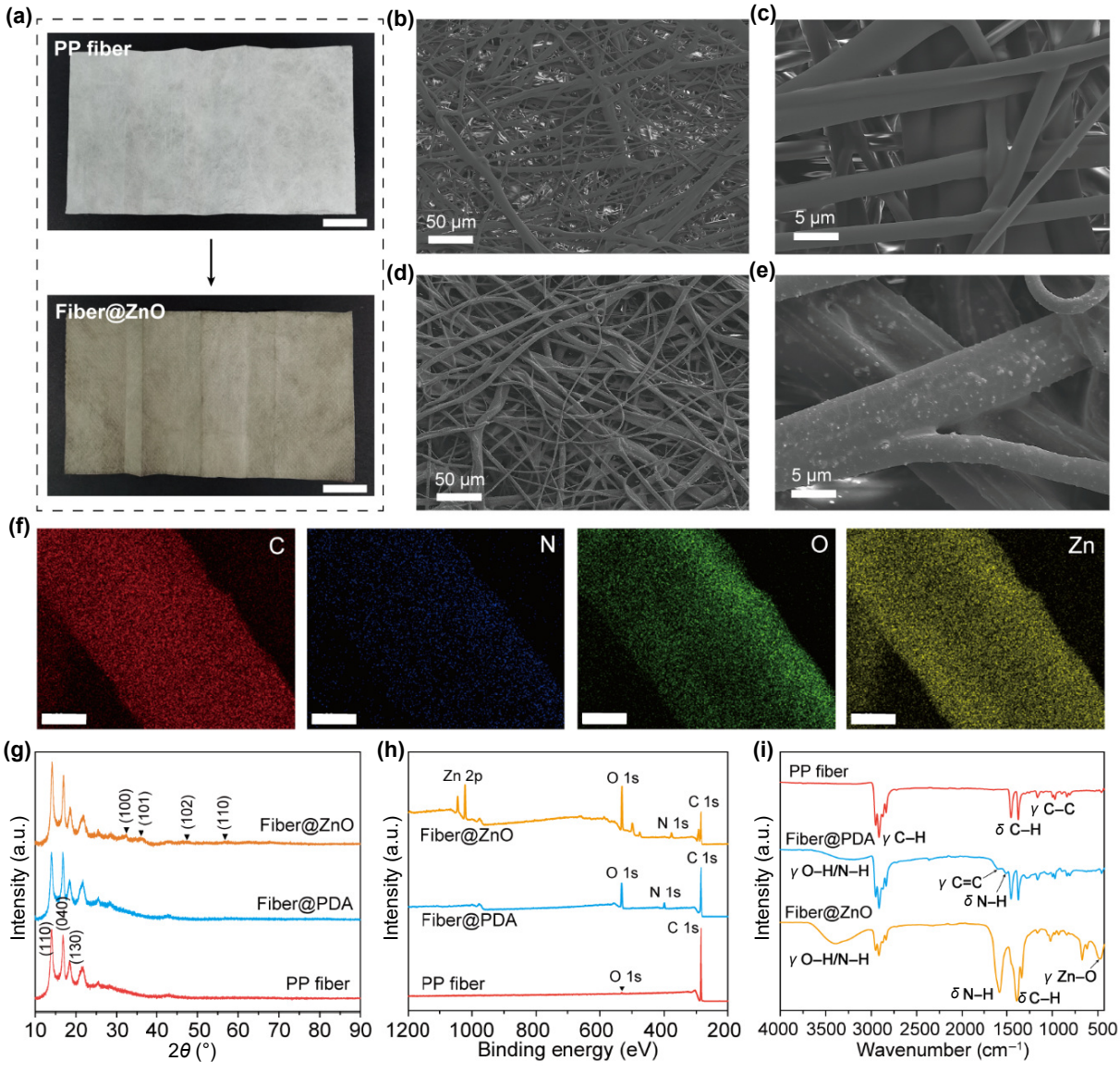

Figure 2 (a) Digital photographs of the pristine PP fiber and fiber@ZnO composite membrane under visible light (the scale bar is 2 cm). (b) SEM image of the PP fibers at low magnification. (c) The enlarged SEM image of the PP fibers. (d) SEM image of the fiber@ZnO at low magnification. (e) The enlarged SEM image of the fiber@ZnO. (f) EDS mapping images of C, N, O, and Zn elements of the fiber@ZnO. (g) XRD patterns of the pristine PP fiber, fiber@PDA, and fiber@ZnO. (h) The XPS spectra of the pristine PP fiber, fiber@PDA, and fiber@ZnO. (i) FITR spectra of the pristine PP fiber, fiber@PDA, and fiber@ZnO.

The chemical composition and structure of the pristine and modified PP fibers were further analyzed using XRD, XPS, and FTIR spectra. XRD spectra are shown in Fig. 2(g), the characteristic diffraction peaks of PP fiber appear at 14.1°, 16.8°, and 18.6°, corresponding to the (110), (040), and (130) crystal planes, respectively [42]. In contrast, there is no obvious difference between the diffraction peaks of fiber@PDA and pristine PP fibers, indicating that PDA treatment does not affect the crystal structure of the PP fiber. Although there are no prominent diffraction peaks of ZnO in fiber@ZnO due to the low content of NPs, the diffraction peaks corresponding to wurtzite ZnO can still be observed (JCPDS 89-1397) [40], indicating the successful deposition of NPs. The XPS spectra of the three fibers are shown in Fig. 2(h). Only the C 1s and O 1s peaks are detected for the pristine PP fiber. However, the characteristic N 1s peak can be observed after the decoration with PDA coating on the surface of the PP fibers, which is assigned to the amino groups in PDA [43, 44]. The high-resolution XPS spectra of the Zn 2p are shown in Fig. S6 in the ESM. The spectrum of Zn 2p consists of two individual peaks at 1021.33 and 1044.41 eV, corresponding to the binding energy of Zn $2p_{3/2}$ and Zn $2p_{1/2}$, respectively. This demonstrates the existence of Zn in the form of ZnO. This result also indicates the successful loading of ZnO NPs onto the fiber@ZnO [37]. The high-resolution C 1s spectra are shown in Fig. S7 in the ESM. The C 1s envelope of the fiber@PDA and fiber@ZnO can be deconvoluted into three Gaussian peaks corresponding to C–C/C–H, C–N/C–O, and C=O, respectively [45, 46]. XPS spectra reveal that the addition of ZnO NPs induces a change in the chemical environment. The absence of new covalent bonds in the C 1s spectra indicates that the shift is attributed to weak interactions. For example, the peak of C–N/C–O at 285.74 eV in the fiber@PDA shifts to a lower binding energy of 285.49 eV in the fiber@ZnO, potentially indicating the formation of hydrogen bonds between ZnO NPs and PDA [47, 48]. Figure 2(i) shows the FTIR spectra of PP fiber before and after modification. The three curves exhibit a bending vibration peak of $-CH_3$ at 1454 cm^{-1}, and there are various forms of tensile vibration of $-CH_2$ and $-CH_3$ in the range of 2900–2960 cm^{-1}, the peak at 997 cm^{-1} is the stretching vibration of the C–C in the polymer, these absorption peaks are all characteristic peaks of PP fiber [49]. While after being modified with PDA, the absorption peak of C=C appearing at 1595 cm^{-1} is related to the vibration of the aromatic ring in PDA, the absorption peak at 1508 cm^{-1} ascribed to the bending vibration of N–H, and the wider absorption peaks in the range of 3100–3300 cm^{-1} are attributed to the stretching vibration of N–H and O–H of PDA [50, 51]. These characteristic absorption peaks represent the functional groups on PDA, demonstrating the successful coating of PDA on the surface of the PP fibers. Furthermore, the absorption peak of fiber@ZnO at 475 cm^{-1} can be attributed to the stretching vibration of Zn–O, and the broader absorption peaks in the range of 3200–3500 cm^{-1} are associated with the stretching vibration of N–H and O–H, which indicate that the NPs are successfully attached on the fiber@ZnO composite membrane surface [37]. After incorporating NPs, the vibrational peak of the O–H shifts from 3250 to 3390 cm^{-1}, the vibrational peak of the Zn–O shifts from 451 to 475 cm^{-1}, which may be related to the formation of hydrogen bonds between ZnO NPs and PDA [52]. All the above results clearly show that hydrogen bonding interaction plays a key role in the formation of the fiber@ZnO composite membrane.

3.4 Antibacterial and antiviral properties and antibacterial mechanism of the fiber@ZnO composite membrane

As the antibacterial filter layer of the mask, it is necessary to test fiber@ZnO for its effectiveness against bacteria and viruses associated with respiratory diseases, which will facilitate its practical application. *S. aureus* is a major pathogen of respiratory diseases, particularly in immunocompromised individuals and following influenza, where it often causes severe pneumonia, empyema, upper respiratory infections, and other complications. *E. coli*, primarily an enteric pathogen, can occasionally cause respiratory infections in immunosuppressed patients or hospital settings, especially hospital-acquired pneumonia and septic pneumonia. For this reason, *S. aureus* and *E. coli* were selected as the representatives of Gram-positive bacteria and Gram-negative bacteria among the bacterial populations associated with respiratory diseases, and the antibacterial properties and bactericidal mechanism of the fiber@ZnO composite membrane were investigated. Primarily, the antibacterial properties of three types of fibers (fiber@ZnO-0.1, fiber@ZnO-0.5, fiber@ZnO-1.0) were evaluated to investigate the relationship between ZnO NPs concentration and the antibacterial properties of fiber@ZnO. In the EDS image (Fig. S8 in the ESM), the content of ZnO on the fiber@ZnO increases with the increase of the concentration of ZnO impregnation solution. The antibacterial results of the PP fiber and three types of fiber@ZnO against *S. aureus* and *E. coli* are shown in Fig. 3(a) and Fig. S9 in the ESM. It can be seen that the bacterial survival rates of the pristine PP fiber and blank control groups were nearly identical. In contrast, the bacterial survival rate decreased significantly after treatment with fiber@ZnO composite membrane. When the concentration of ZnO NPs impregnating solution reached 1.0 mg/mL, the fiber@ZnO composite membrane achieves a ZnO NPs content of 6.5% (Fig. 2(h)), the bactericidal rate of fiber@ZnO against *S. aureus* and *E. coli* exceeded 99%, indicating excellent broad-spectrum antibacterial activities. And, the antibacterial results of the fiber@PDA are shown in Fig. S10 in the ESM. It can be seen that the bactericidal rates of the fiber@PDA against *S. aureus* and *E. coli* are both less than 50%, indicating that the PDA coating has limited contribution to the antibacterial properties of the fiber@ZnO and has almost no effect. This also further illustrates the role of ZnO NPs as an antibacterial agent for the fiber@ZnO. Meanwhile, ZnO NPs and fiber@ZnO can also effectively inhibit the growth of H1N1 virus, with a log inactivation value greater than 4.0 and a corresponding virus inactivation rate of up to 99.99%, demonstrating excellent antiviral performance (Fig. S11 in the ESM).

Furthermore, the inhibitory effects of fiber@ZnO composite membrane on bacterial growth were measured through a growth inhibition assay, and the OD_{600} values were recorded over 10 h. Normally, there is a notable tendency for *S. aureus* and *E. coli* to grow over time, with the OD_{600} value at the stationary phase significantly increasing from 0.03 to 0.78 and 0.66, respectively. In contrast, the growth curve of *S. aureus* and *E. coli* treated with fiber@ZnO composite membrane are similar to that of the blank control group (only fiber@ZnO in the LB solution), no bacteria cell growth occurs during 10 h cultivation, indicating that the fiber@ZnO composite membrane significantly inhibits bacterial growth. Additionally, the antibacterial performance of the fiber@ZnO composite membrane was measured through live/dead fluorescence assays and flat counts of bacteria. The fluorescent nucleic acid dyes SYTO 9 and PI have different penetrability in healthy microbial cells. SYTO 9 nucleic acid dye labels all bacteria and emits green fluorescence, while PI nucleic acid dye labels only bacteria with damaged membranes and emits red fluorescence.

Therefore, green fluorescence is dominant in normal cells, while cells with damaged membranes exhibit distinct red fluorescence [53]. As shown in Fig. 3(c) and Fig. S12 in the ESM, almost all cells are stained green both for the control group and after treatment with the pristine PP fibers, indicating that the bacterial cells are alive and that the pristine PP fibers have less inhibitory effect on bacterial growth. In contrast, the merged image of the fiber@ZnO is dominated by red fluorescence and almost without any green fluorescence, indicating that the fiber@ZnO composite membrane could inactive *S. aureus* and *E. coli*. Meanwhile, images of the flat counting of *S. aureus* and *E. coli* treated by the pristine PP fibers and fiber@ZnO composite membrane also reflected the results of antibacterial activities (Fig. 3(d)). The above results indicate that the fiber@ZnO composite membrane exhibits excellent broad-spectrum antibacterial and antiviral activity.

It is commonly reported that the bactericidal mechanism of ZnO NPs is primarily attributed to the released zinc ions, the generation of ROS, and the interaction of the NPs with the bacterial surface [37]. Our previous work has reported that ZnO NPs did not effectively kill bacteria by releasing sufficient zinc ions [54]. Therefore, zinc ions are not the bactericidal factor of the fiber@ZnO composite membrane in this case. Then, the content of ROS in the fiber@ZnO and ZnO NPs solution was measured by electron paramagnetic resonance (EPR) using 5,5-dimethyl-1-pyrroline-N-oxide (DMPO) and 2,2,6,6-tetramethylpiperidine-1-oxyl (TEMP) as spin probes [55, 56]. As shown in Fig. 3(e) and Fig. S13 in the ESM, there is obvious signals can be observed, which are assigned to $^1O_2$, ·OH, and $\cdot O_2^-$, and the types of ROS generated by the fiber@ZnO are the same as those produced by ZnO NPs. The generation of reactive oxygen species (ROS) is a key mechanism behind the antibacterial properties of ZnO NPs. Hydroxyl radicals and superoxide anions are highly reactive oxidants that attack the lipid bilayer of the bacterial membrane, leading to lipid peroxidation and increased membrane permeability. ROS can also oxidize thiol groups on membrane and intracellular proteins, resulting in protein denaturation and loss of function. Moreover, ROS can cause DNA strand breaks or base modifications, disrupting gene expression and cell division. The multifaceted actions of ROS are often synergistic, with different types of ROS targeting different regions of the bacteria. Ultimately, these effects compromise bacterial survival. ROS can also destroy viral proteins and nucleic acids, resulting in the fiber@ZnO composite membrane exhibiting excellent antiviral activity [33, 36].

Furthermore, *S. aureus* and *E. coli* respond differently to ROS and electrostatic interactions due to their structural differences [34]. The thick peptidoglycan layer in *S. aureus* slows ROS penetration, leading to cumulative damage over time, while *E. coli*'s thinner outer membrane allows faster ROS penetration, causing acute damage. Structurally, the peptidoglycan layer of *S. aureus* contains numerous amino acid side chains and polyanions (such as teichoic

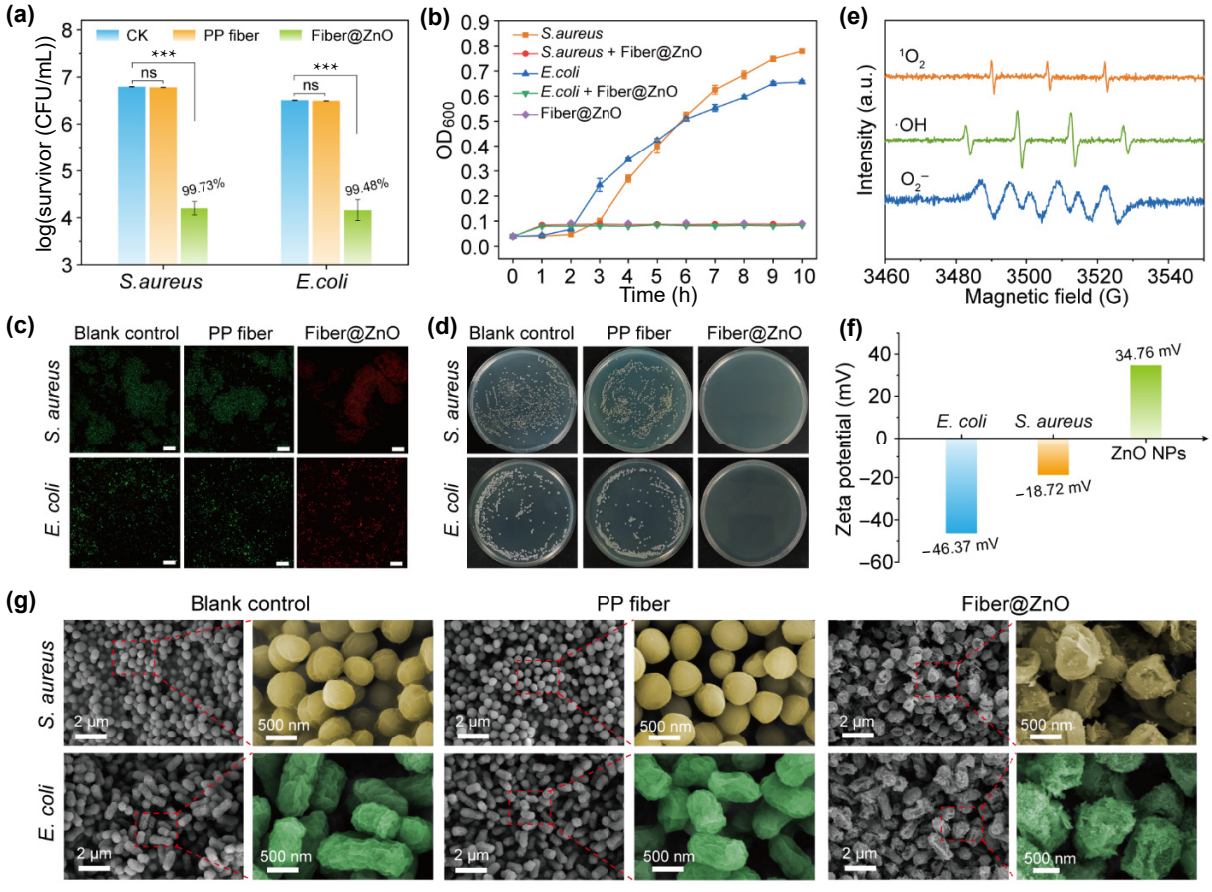

Figure 3 (a) Log survivor of *S. aureus* and *E. coli* after treatment with the pristine PP fiber and fiber@ZnO. (b) Growth curve of *S. aureus* and *E. coli* after treatment with the fiber@ZnO. (c) The merge CLSM images of bacteria stained by SYTO 9 and PI, respectively (the scale bar is 10 μm). (d) Flat counting images of *S. aureus* and *E. coli* after treatment with the pristine PP fiber and fiber@ZnO. (e) EPR spectra of the ZnO NPs for detection of ROS. (f) The zeta potential of the ZnO NPs, *S. aureus*, and *E. coli*. (g) SEM images of *S. aureus* and *E. coli* after treatment with the pristine PP fiber and fiber@ZnO. The data are presented as means ± SDs. $p > 0.05$ (non significant), $^*p < 0.05$, $^{**}p < 0.01$, and $^{***}p < 0.001$.

acids), giving its surface a weak negative charge. As a result, electrostatic adsorption between *S. aureus* and ZnO NPs is relatively weak, making the contribution of electrostatic interactions to the bactericidal effect limited. On the other hand, the phosphate and carboxyl groups in the peptidoglycan layer of *E. coli* confer a higher negative charge density to its surface, resulting in stronger electrostatic adsorption with ZnO NPs [35]. Then, zeta potential measurements were used to quantify the electrostatic interaction strength between ZnO NPs and bacterial surfaces, validating the differences. Figure 3(f) illustrates these differences, showing a greater zeta potential disparity between *E. coli* and ZnO (−46.37 mV vs. 34.76 mV) compared to *S. aureus* and ZnO (−18.72 mV vs. 34.76 mV). This confirms that electrostatic interactions are stronger for *E. coli* and ZnO NPs. To verify whether the integrity of the bacterial cell membrane could be disrupted by the electrostatic interaction between NPs and bacteria, the bacterial morphology with pristine PP fiber and fiber@ZnO composite membrane treatment was observed by SEM. As shown in Fig. 3(g), compared with the intact bacterial cell membrane and normal morphology in the control group and after treatment with pristine PP fiber, there was a significant change in the cell membrane and shape of bacteria after treatment with the fiber@ZnO composite membrane, indicating that the electrostatic interaction between ZnO NPs and bacteria can kill bacteria by destroying cell structures. In conclusion, the antibacterial action against *S. aureus* primarily depends on ROS-driven cumulative damage, whereas *E. coli* exhibits a synergistic mechanism involving both ROS and electrostatic interactions.

3.5 Biocompatibility and performance stability of fiber@ZnO composite membrane

The Anti-moisture parameters are key factor influencing mask comfort. The water contact angle of the PP fiber is around 130°, indicating its hydrophobic nature. Due to hydrophilicity of the PDA film and ZnO NPs, the water contact angle of the fiber@ZnO decreases by about 12% to 117° (Fig. 4(a)). Despite this reduction, fiber@ZnO remains hydrophobic, which is beneficial for maintaining mask comfort. Additionally, weight gain experiments in humid environments for fiber@ZnO were also investigated. The weight change of the PP fiber, fiber@PDA and fiber@ZnO were measured after being placed for 12 h using saturated salt solutions as the humidity source. Different relative humidity levels were obtained by dissolving LiCl (RH 11%), $C_2H_3KO_2$ (RH 23%), K_2CO_3 (RH 43%), NaBr (RH 57%), KI (RH 69%), NaCl (RH 75%), KCl (RH 84%), and KNO_3 (RH 94%) into deionized water in closed glass containers at 25 °C [57]. As shown in Fig. 4(b), under the humidity conditions of the living environment (about 40%–60%),

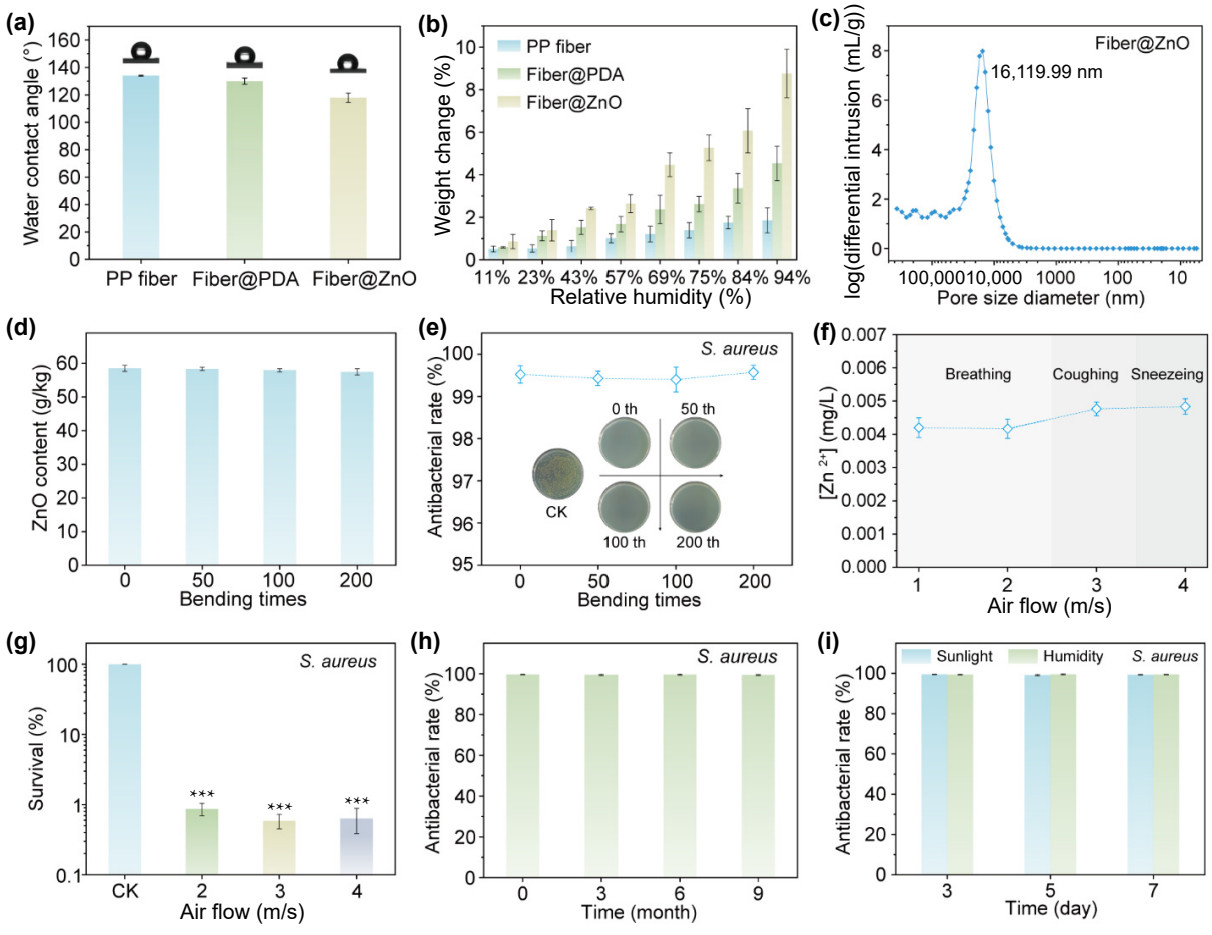

Figure 4 (a) Water contact angle of the PP fiber, fiber@PDA and fiber@ZnO. (b) Weight gain experiments of the PP fiber, fiber@PDA and fiber@ZnO under different humidity environments. (c) Pore size distribution curves for the fiber@ZnO. (d) The changes in ZnO loading of fiber@ZnO composite membrane after continuous bending. (e) The changes in antibacterial properties of fiber@ZnO composite membrane after continuous bending. (f) The shedding amount of ZnO NPs from fiber@ZnO composite membrane under different air flows. (g) Antibacterial performance of fiber@ZnO composite membranes after treatment with different airflows. (h) Antibacterial rate of fiber@ZnO composite membranes after being placed at different times. (i) The antibacterial performance of the fiber@ZnO composite membranes in different environments for different times. The data are presented as means ± SDs. $p > 0.05$ (non significant), $^{*}p < 0.05$, $^{**}p < 0.01$, and $^{***}p < 0.001$.

the weight change of the fiber@ZnO is relatively small (about 3%) compared to the PP fiber. This indicates that ZnO NPs and PDA modification have mminimal impact on the wettability of PP fiber. As shown in Fig. 4(c) and Fig. S14 in the ESM, the pore size of the original PP fiber membrane decreased slightly from 16,485 to 16,119 nm after modification, with a reduction of approximately 2%. This small change indicates minimal impact on surface roughness, with no significant rearrangement or densification, suggesting that roughness changes contributed little to the observed decrease in contact angle [58]. The decrease from 134° to 117° was primarily driven by chemical modifications, as the polydopamine coatings and ZnO introduced hydrophilic groups (–OH and $–NH_2$) on the fiber surface. Additionally, the slight pore size reduction may have enhanced capillary effects and increased the liquid–solid contact area, further supporting the reduction in the contact angle [59].

The fiber@ZnO composite membranes are used as the filter layer of antibacterial masks. Thus, it is valuable to investigate the stable attachment of NPs to fiber@ZnO and the changes in the properties of PP fiber before and after modification. Primarily, the adhesion stability of NPs was evaluated by measuring the changes in weight and NPs loading of the fiber@ZnO composite membrane after physical bending. As shown in Video ESM1, after multiple bends, the morphological changes of PP fiber and fiber@ZnO become consistent, and no damage occurs, demonstrating the stability of the fiber@ZnO and its ability to maintain structural integrity under external forces. At the same time, fiber@ZnO withstood bending and twisting 200 times with negligible weight loss (Fig. S15 in the ESM), and the reduction of ZnO loading exhibited minimal changes compared to the blank control group (Fig. 4(d)). The decrease is nearly negligible, verifying the outstanding attachment stability of the NPs in the fiber@ZnO composite membranes. Moreover, the fiber@ZnO composite membranes still have excellent antibacterial properties after treatment with different bending times, with an antibacterial rate of more than 99% (Fig. 4(e)). In addition, masks are used in contact with the mouth and nose, and there is airflow during normal respiration. Therefore, it is essential to assess whether the NPs are stably attached within the fiber@ZnO composite membrane under different airflow conditions to determine any potential inhalation risks. For this purpose, it was evaluated whether NPs detached from the fiber@ZnO composite membrane (about 0.2 g) in an airflow of 20 min with speeds ranging from 1 to 4 m/s (Fig. S16 in the ESM), which were used to simulate the airflow conditions corresponding to normal human breathing (1–2 m/s), coughing (3 m/s), and sneezing (4 m/s) [1]. As shown in Fig. 4(f), under all airflow conditions, the shedding of ZnO NPs was minimal compared to their original loading on the fiber@ZnO composite membranes. The total shedding amount of ZnO NPs from fiber@ZnO under human breath conditions over time was also investigated. To this end, we simulated typical mask-wearing conditions for about 6 h and evaluated the total ZnO NPs shedding over different time intervals (fiber@ZnO weight: 0.8 g, air flow: 4 m/s, liquid volume in the experimental setup: 1000 mL). As shown in Fig. S17 in the ESM, at a air fiow greater than normal breathing, the total amount of ZnO NPs shedding in 6 h is about 0.18 mg/L, accounting for about 0.34% of the total amount of ZnO NPs on the fiber@ZnO composite membrane. This result indicates that under normal human breathing conditions, the shedding of ZnO NPs is negligible, demonstrating good biosafety of the mask. The antibacterial activity of the fiber@ZnO composite membrane after treatment with different air flows is shown in Fig. 4(g), the bacterial survival rate is less than 1%, and the corresponding bactericidal rate can reach 99%, showing excellent antibacterial activity and good stability. Meanwhile, the fiber@ZnO composite membranes were still able to maintain a bactericidal rate of 99% after nine months of storage, indicating excellent antibacterial stability (Fig. 4(h)). After exposure to sunlight and humidity for varying periods, the antibacterial properties are almost unchanged compared with the original fabric, as illustrated in Fig. 4(i). The SEM and EDS images of the fiber@ZnO after five and ten antimicrobial cycles are shown in Fig. S18 in the ESM. From four different viewing angles, it can be seen that the morphology of fiber@ZnO remains largely unchanged after repeated use, and ZnO NPs are still well-distributed on surface, demonstrating excellent stability. Furthermore, the antibacterial performance was assessed, as shown in Fig. S19 in the ESM. The results indicate that the antibacterial properties of fiber@ZnO remain largely unchanged, with no significant decline in its efficacy. Taken together, these results demonstrate the good stability and reusability of the fiber@ZnO. Meanwhile, we also examined the degree of bacterial adhesion on the fiber@ZnO surface using SEM images after cyclic antibacterial experiment. As shown in Fig. S20 in the ESM, even after 5 and 10 cycles of testing, only a small amount of bacteria was observed on the fiber@ZnO surface across four different fields of view. This indicate that material resists bacterial attachment effectively, potentially due to its hydrophobicity (as demonstrated in Fig. 4(a)). Although it remains challenging to determine whether the reduced bacterial presence is solely due to spontaneous detachment or the intrinsic hydrophobic nature of the fiber@ZnO, the results collectively indicate excellent self-cleaning performance.

Furthermore, it is necessary to evaluate the biocompatibility of the fiber@ZnO in terms of practical application. To ensure the safety of the fiber@ZnO, we conducted a cell safety test using Hela cells as the model. The survival rates of Hela cells were statistically analyzed after treatment with different types, including PP fiber, fiber@ZnO-0.1, fiber@ZnO-0.5, and fiber@ZnO-1.0. In the experiment, the cells were first treated with the fiber for 2 and 4 h to simulate the typical mask usage durations in daily life. After that, the cells were incubated for 24 or 48 h before being counted and analyzed. As shown in Fig. S21 in the ESM, we tested the proliferation of Hela cells coincubated with different types of fiber using Cell Counting Kit-8 (CCK-8) assay. Compared with the control group, fiber@ZnO has minimal effect on cell proliferation whitin 48 h, with Hela cells viability remaining above 80%. The result indicates that the fiber@ZnO exhibits excellent biocompatibility and low toxicity. Then, the impact of the modification strategy on the mechanical properties and air permeability of the PP fiber was evaluated. The mechanical strength of the pristine PP fiber and fiber@ZnO composite membrane was evaluated by stress-stain test, as shown in Fig. S22 in the ESM. The breaking strength of fiber@ZnO composite membrane decreases by 9.4% from 5.19 to 4.70 MPa, which is a slight decrease compared to the pristine PP fiber, and it may be related to the alkaline environment during the surface modification process. Similarly, the air permeability of fiber@ZnO composite membrane also decreases by 8.9% from 146 to 133 mm/s (Fig. S23 in the ESM), which may be attributed to the increase in the diameter of PP fiber caused by PDA treatment, consequently affecting the porosity of the fiber membrane. Although the breaking strength and air permeability of fiber@ZnO composite membrane are slightly lower than those of the pristine PP fiber, it does not affect its use as a filter layer in

antibacterial masks. Collectively, these results indicated that fiber@ZnO composite membrane exhibits a relatively stable physical performance, which should facilitate its potential application as an antibacterial layer in a mask.

3.6 Application of the fiber@ZnO composite membrane in N95 mask

Typically, the spread of pathogens from one person to another through aerosols leads to the occurrence of respiratory diseases. As a proof of concept, we demonstrated the potential application of fiber@ZnO composite membranes in a mask. The fiber@ZnO mask is a multilayered mask with composite fiber membranes as a middle antibacterial layer sandwiched between the first two layers of a commercial N95 mask (Fig. 5(a)). The self-cleaning performance of the fiber@ZnO mask was assessed by comparing its antibacterial activity with that of a commercial N95 mask. As shown in Fig. S24 in the ESM and Fig. 5(a), the fiber@ZnO mask and commercial N95 mask were exposed to artificial pathogenic aerosols generated from bacteria suspensions for 10 min [1, 9]. The number of residual *E. coli* cells on the masks and the corresponding colony count images are presented in Figs. 5(b)–5(d). It can be seen that although a considerable number of living bacteria are visible on the first layers of all masks, the count of living bacterial cells significantly decreased, with nearly undetectable levels on the second and third layers of the fiber@ZnO mask compared to the commercial N95 mask. Simultaneously, the residual levels of *S. aureus* on the mask are similar to that of *E. coli*, and the antibacterial layer of the fiber@ZnO mask exhibits an excellent bacteria inactivation effect (Figs. 5(e)–5(g)). Obviously, the fiber@ZnO mask demonstrated superior bactericidal performance compared to the commercial N95 mask. The excellent self-cleaning performance indicates the great application potential for the fiber@ZnO mask.

4 Conclusions

In summary, a simple and general biomimetic surface modification strategies has been developed for the fabrication of self-cleaning antibacterial mask based on the as-prepared fiber@ZnO composite membranes. The hydrogen bonding interaction and electrostatic interaction between ZnO NPs and PDA was used to establish a stable association of NPs and PP fibers, which endows the fiber@ZnO composite membrane with spontaneous and sustained broad-spectrum antibacterial and antiviral activity. The synergistic effect of electrostatic interaction and ROS play a key role in bacterial and virus inactivation, with a bactericidal rate greater than 99% against both Gram-positive (*S. aureus*) and Gram-negative (*E. coli*) bacteria, and exhibits an inhibition rate exceeding 99.99% against the H1N1 influenza virus. Furthermore, fiber@ZnO masks exhibit superior self-cleaning performance and effectively kill pathogenic bacteria in aerosols compared with commercial N95

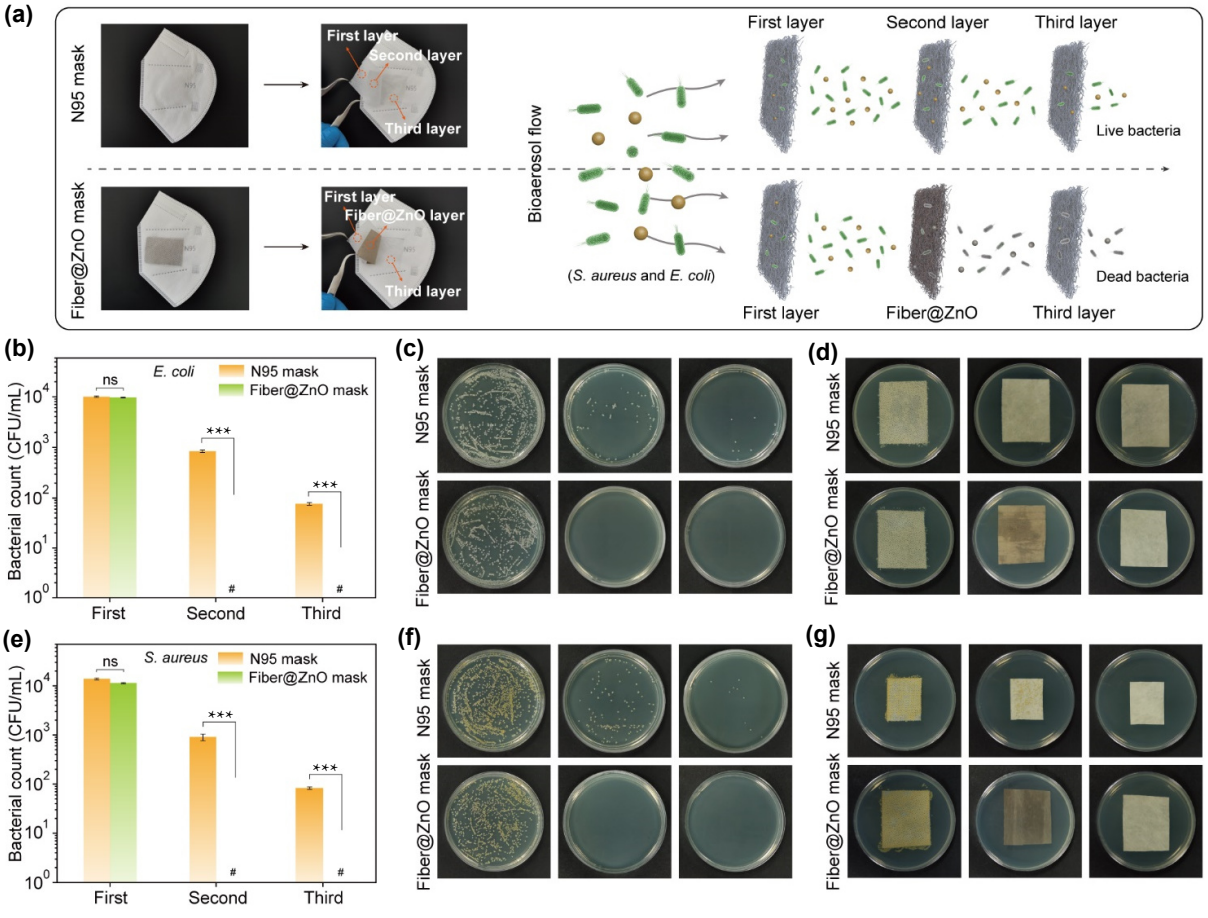

Figure 5 (a) Digital photographs of commercial N95 mask and fiber@ZnO mask (left) and the schematic illustration of commercial N95 mask and fiber@ZnO mask inactivating bacteria in aerosols (right). (b) The number of viable bacteria and (c) colony count images on each layer of the mask after the reaction. (d) Colony counts images of *E. coli* residual on the eluent-treated mask. (e) The number of viable bacteria and (f) colony count images on each layer of the mask after reaction. (g) Colony counts images of *S. aureus* residual on the eluent-treated mask. The data are presented as means ± SDs. $p > 0.05$ (non significant), $^{*}p < 0.05$, $^{**}p < 0.01$, and $^{***}p < 0.001$.

masks. This study not only offers an effective strategy for developing antibacterial masks but also demonstrates significant potential applications in reducing the risk of human infection and preventing the re-transmission of pathogens.

Electronic Supplementary Material: Supplementary material (TEM image, FTIR spectra, XRD patterns, PL excitation and emission spectra of ZnO NPs; XPS spectra, EDS spectra, SEM images, pore size and antibacterial properties of fiber@PDA and fiber@ZnO; CLSM images of bacteria; EPR spectra and zeta potential of fiber@ZnO; antiviral activity of ZnO NPs and fiber@ZnO; anti-cytotoxicity of fiber@ZnO; air permeability and breaking strength of PP fiber and fiber@ZnO) is available in the online version of this article at https://doi.org/10.26599/NR.2025.94907205.

Data availability

All data needed to support the conclusions in the paper are presented in the manuscript and the Electronic Supplementary Material. Additional data related to this paper may be requested from the corresponding author upon request.

Acknowledgements

The authors acknowledge the National Natural Science Foundation of China (Nos. 12274378 and 62075198) and Outstanding Youth Foundation of Henan (Nos. 222300420087) for financial support of this work.

Declaration of competing interest

All the contributing authors report no conflict of interests in this work.

Author contribution statement

Y. W.: Conceptualization, experimental design, data curation, validation, writing manuscript. W.-B. Z.: Data curation, validation, experimental design. F.-K. L. and S. L. C.: Validation, experimental design. B.-S. S.: Data curation, experimental design. L. J.: Validation, experimental design. K.-K. L. and C.-X. S.: Conceptualization, supervision, project administration, funding acquisition, writing – review & editing. All the authors have approved the final manuscript.

Informed consent

Not applicable.

Ethics statement

Not applicable.

Use of AI statement

None.

References

[1] Jin, X. Y.; Gao, F.; Qin, M. X.; Yu, Y. P.; Zhao, Y.; Shao, T. Y.; Chen, C.; Zhang, W. H.; Xie, B.; Xiong, Y. J. et al. How to make personal protective equipment spontaneously and continuously antimicrobial (incorporating oxidase-like catalysts). *ACS Nano* **2022**, *16*, 7755–7771.

[2] Qian, J.; Dong, Q.; Chun, K.; Zhu, D. Y.; Zhang, X.; Mao, Y. M.; Culver, J. N.; Tai, S.; German, J. R.; Dean, D. P. et al. Highly stable, antiviral, antibacterial cotton textiles via molecular engineering. *Nat. Nanotechnol.* **2023**, *18*, 168–176.

[3] Wang, Y.; Cao, R.; Wang, C.; Song, X. Y.; Wang, R. N.; Liu, J. C.; Zhang, M. M.; Huang, J. Y.; You, T. T.; Zhang, Y. H. et al. *In situ* embedding hydrogen-bonded organic frameworks nanocrystals in electrospinning nanofibers for ultrastable broad-spectrum antibacterial activity. *Adv. Funct. Mater.* **2023**, *33*, 2214388.

[4] Heng, W. Z.; Yin, S. K.; Min, J. H.; Wang, C. R.; Han, H.; Shirzaei Sani, E.; Li, J. H.; Song, Y.; Rossiter, H. B.; Gao, W. A smart mask for exhaled breath condensate harvesting and analysis. *Science* **2024**, *385*, 954–961.

[5] Zhao, T. N.; Xiao, X.; Wu, Y. C.; Ma, J. J.; Li, Y.; Lu, C. Y.; Shokoohi, C.; Xu, Y. Q.; Zhang, X. M.; Zhang, Y. Z. et al. Tracing the flu symptom progression via a smart face mask. *Nano Lett.* **2023**, *23*, 8960–8969.

[6] Luo, X. M.; Yin, C. Y.; Ji, L. F.; Feng, J. Y.; Zhang, P.; Wang, X. C.; Ma, Y.; Liu, X. H. An antimicrobial polymer brush coating to fabricate high-performance, durable, self-sterilization, and recyclable face masks. *Chem. Mater.* **2023**, *35*, 9245–9256.

[7] Sim, M. T.; Ee, Z. Y.; Lim, Y. H.; Sia, T. S.; Ong, D. T. K.; Koay, J. S. C.; Goh, B. T.; Yong, Y. S.; Aw, K. C.; Tan, S. T. et al. Instant disinfecting face masks utilizing electroporation powered by respiration-driven triboelectric nanogenerators. *Adv. Funct. Mater.* **2024**, *34*, 2410062.

[8] Zhong, H.; Zhu, Z. R.; Lin, J.; Cheung, C. F.; Lu, V. L.; Yan, F.; Chan, C. Y.; Li, G. J. Reusable and recyclable graphene masks with outstanding superhydrophobic and photothermal performances. *ACS Nano* **2020**, *14*, 6213–6221.

[9] Li, P.; Li, J. Z.; Feng, X.; Li, J.; Hao, Y. C.; Zhang, J. W.; Wang, H.; Yin, A. X.; Zhou, J. W.; Ma, X. J. et al. Metal-organic frameworks with photocatalytic bactericidal activity for integrated air cleaning. *Nat. Commun.* **2019**, *10*, 2177.

[10] Huang, L. B.; Xu, S. Y.; Wang, Z. Y.; Xue, K.; Su, J. J.; Song, Y.; Chen, S. J.; Zhu, C. L.; Tang, B. Z.; Ye, R. Q. Self-reporting and photothermally enhanced rapid bacterial killing on a laser-induced graphene mask. *ACS Nano* **2020**, *14*, 12045–12053.

[11] Yu, D. M.; Liu, L. F.; Yu, J. Y.; Si, Y.; Ding, B. Meta-aerogel electric trap enables instant and continuable pathogen killing in face masks. *ACS Nano* **2023**, *17*, 20601–20610.

[12] Cimini, A.; Imperi, E.; Picano, A.; Rossi, M. Electrospun nanofibers for medical face mask with protection capabilities against viruses: State of the art and perspective for industrial scale-up. *Appl. Mater. Today* **2023**, *32*, 101833.

[13] Huang, H. Y.; Park, H.; Liu, Y. H.; Huang, J. X. On-mask chemical modulation of respiratory droplets. *Matter* **2020**, *3*, 1791–1810.

[14] Park, S. J.; Lee, C. H.; Kim, Y.; Ko, J. H.; Kim, T.; Kim, S. J.; Nahm, S.; Cho, H.; Moon, M. W. M. Multiscale landscaping of droplet wettability on fibrous layers of facial masks. *Proc. Natl. Acad. Sci. USA* **2022**, *119*, e2209586119.

[15] Peng, Z. H.; Shi, J. H.; Xiao, X.; Hong, Y.; Li, X. M.; Zhang, W. W.; Cheng, Y. L.; Wang, Z. K.; Li, W. J.; Chen, J. et al. Self-charging electrostatic face masks leveraging triboelectrification for prolonged air filtration. *Nat. Commun.* **2022**, *13*, 7835.

[16] Tuñón-Molina, A.; Takayama, K.; Redwan, E. M.; Uversky, V. N.; Andrés, J.; Serrano-Aroca, Á. Protective face masks: Current status and future trends. *ACS Appl. Mater. Interfaces* **2021**, *13*, 56725–56751.

[17] Wang, Q. F.; Wei, Y. Z.; Li, W. B.; Luo, X. Z.; Zhang, X. Y.; Di, J. C.; Wang, G. Q.; Yu, J. H. Polarity-dominated Stable N97 respirators for airborne virus capture based on nanofibrous membranes. *Angew.*

Chem., Int. Ed. **2021**, *60*, 23756–23762.
[18] Zhou, Z. Q.; Wang, D.; Pan, Z. Y.; You, T. L.; Xu, G. L.; Liang, Y.; Tang, M. Bioinspired structures made of silicone nanofilaments for upcycling waste masks to reusable N95 respirators. *Nano Lett.* **2024**, *24*, 4415–4422.
[19] Chen, M. X.; Hu, Q.; Wang, X. Y.; Zhang, W. A review on recent trends of the antibacterial nonwovens air filter materials: Classification, fabrication, and application. *Sep. Purif. Technol.* **2024**, *330*, 125404.
[20] Deng, W.; Sun, Y. J.; Yao, X. X.; Subramanian, K.; Ling, C.; Wang, H. B.; Chopra, S. S.; Xu, B. B.; Wang, J. X.; Chen, J. F. et al. Masks for COVID-19. *Adv. Sci.* **2022**, *9*, 2102189.
[21] Pullangott, G.; Kannan, U.; S, G.; Kiran, D. V.; Maliyekkal, S. M. A comprehensive review on antimicrobial face masks: An emerging weapon in fighting pandemics. *RSC Adv.* **2021**, *11*, 6544–6576.
[22] Hossain, T.; Shahid, A.; Mahmud, N.; Habib, A.; Rana, M.; Khan, S. A.; Hossain, D. Research and application of polypropylene: A review. *Discover Nano* **2024**, *19*, 2.
[23] Gao, J. F.; Luo, J. C.; Wang, L.; Huang, X. W.; Wang, H.; Song, X.; Hu, M. J.; Tang, L. C.; Xue, H. G. Flexible, superhydrophobic and highly conductive composite based on non-woven polypropylene fabric for electromagnetic interference shielding. *Chem. Eng. J.* **2019**, *364*, 493–502.
[24] Yaman, N.; Özdoğan, E.; Seventekin, N.; Ayhan, H. Plasma treatment of polypropylene fabric for improved dyeability with soluble textile dyestuff. *Appl. Surf. Sci.* **2009**, *255*, 6764–6770.
[25] Cheng, W.; Zeng, X. W.; Chen, H. Z.; Li, Z. M.; Zeng, W. F.; Mei, L.; Zhao, Y. L. Versatile polydopamine platforms: Synthesis and promising applications for surface modification and advanced nanomedicine. *ACS Nano* **2019**, *13*, 8537–8565.
[26] Liu, Y. L.; Ai, K. L.; Lu, L. H. Polydopamine and its derivative materials: Synthesis and promising applications in energy, environmental, and biomedical fields. *Chem. Rev.* **2014**, *114*, 5057–5115.
[27] Yu, J.; Wei, W.; Danner, E.; Ashley, R. K.; Israelachvili, J. N.; Waite, J. H. Mussel protein adhesion depends on interprotein thiol-mediated redox modulation. *Nat. Chem. Biol.* **2011**, *7*, 588–590.
[28] Ma, Z. W.; Feng, J. B.; Huo, S. Q.; Sun, Z. Q.; Bourbigot, S.; Wang, H.; Gao, J. F.; Tang, L. C.; Zheng, W.; Song, P. A. Mussel-inspired, self-healing, highly effective fully polymeric fire-retardant coatings enabled by group synergy. *Adv. Mater.* **2024**, *36*, 2410453.
[29] Fu, Y.; Yang, L.; Zhang, J. H.; Hu, J. F.; Duan, G. G.; Liu, X. H.; Li, Y. W.; Gu, Z. P. Polydopamine antibacterial materials. *Mater. Horiz.* **2021**, *8*, 1618–1633.
[30] Faure, E.; Falentin-Daudré, C.; Jérôme, C.; Lyskawa, J.; Fournier, D.; Woisel, P.; Detrembleur, C. Catechols as versatile platforms in polymer chemistry. *Prog. Polym. Sci.* **2013**, *38*, 236–270.
[31] Lee, H.; Dellatore, S. M.; Miller, W. M.; Messersmith, P. B. Mussel-inspired surface chemistry for multifunctional coatings. *Science* **2007**, *318*, 426–430.
[32] Zhang, W.; Wang, R. X.; Sun, Z. M.; Zhu, X. W.; Zhao, Q.; Zhang, T. F.; Cholewinski, A.; Yang, F.; Zhao, B. X.; Pinnaratip, R. et al. Catechol-functionalized hydrogels: Biomimetic design, adhesion mechanism, and biomedical applications. *Chem. Soc. Rev.* **2020**, *49*, 433–464.
[33] Borisov, V. B.; Siletsky, S. A.; Nastasi, M. R.; Forte, E. ROS defense systems and terminal oxidases in bacteria. *Antioxidants* **2021**, *10*, 839.
[34] Makabenta, J. M. V.; Nabawy, A.; Li, C. H.; Schmidt-Malan, S.; Patel, R.; Rotello, V. M. Nanomaterial-based therapeutics for antibiotic-resistant bacterial infections. *Nat. Rev. Microbiol.* **2021**, *19*, 23–36.
[35] Xie, M. M.; Gao, M.; Yun, Y.; Malmsten, M.; Rotello, V. M.; Zboril, R.; Akhavan, O.; Kraskouski, A.; Amalraj, J.; Cai, X. M. et al. Antibacterial nanomaterials: Mechanisms, impacts on antimicrobial resistance and design principles. *Angew. Chem., Int. Ed.* **2023**, *62*, e202217345.
[36] Zhang, J. K.; Su, P. D.; Chen, H. H.; Qiao, M.; Yang, B.; Zhao, X. Impact of reactive oxygen species on cell activity and structural integrity of Gram-positive and Gram-negative bacteria in electrochemical disinfection system. *Chem. Eng. J.* **2023**, *451*, 138879.
[37] Wang, Y.; Zhao, W. B.; Li, F. K.; Chang, S. L.; Cao, Q.; Guo, R.; Song, S. Y.; Liu, K. K.; Shan, C. X. Engineering sizable and broad-spectrum antibacterial fabrics through hydrogen bonding interaction and electrostatic interaction. *ACS Appl. Mater. Interfaces* **2024**, *16*, 8321–8332.
[38] Wang, Y.; Liu, K. K.; Zhao, W. B.; Sun, J. L.; Chen, X. X.; Zhang, L. L.; Cao, Q.; Zhou, R.; Dong, L.; Shan, C. X. Antibacterial fabrics based on synergy of piezoelectric effect and physical interaction. *Nano Today* **2023**, *48*, 101737.
[39] Jiang, L. Y.; Zhang, S. F.; Liang, Y. C.; Zhou, Y. C.; Shao, H. C.; Wang, H. Y.; Liu, K. K.; Shan, C. X. Advancing programmable information encryption circuits through colorful phosphorescent carbon nanodots with versatile lifetimes. *Adv. Opt. Mater.* **2024**, *12*, 2401494.
[40] Zhao, W. B.; Du, M. R.; Liu, K. K.; Zhou, R.; Ma, R. N.; Jiao, Z.; Zhao, Q.; Shan, C. X. Hydrophilic ZnO nanoparticles@calcium alginate composite for water purification. *ACS Appl. Mater. Interfaces* **2020**, *12*, 13305–13315.
[41] Zhou, R.; Sui, L. Z.; Liu, X. B.; Liu, K. K.; Guo, D. Y.; Zhao, W. B.; Song, S. Y.; Lv, C. F.; Chen, S.; Jiang, T. C. et al. Multiphoton excited singlet/triplet mixed self-trapped exciton emission. *Nat. Commun.* **2023**, *14*, 1310.
[42] Zhu, Y. W.; Sun, Y. J.; Wang, J. L.; Yu, B. R. Antimicrobial and antifouling surfaces through polydopamine bio-inspired coating. *Rare Met.* **2022**, *41*, 499–518.
[43] Zheng, N.; Huang, Y. D.; Sun, W. F.; Du, X. S.; Liu, H. Y.; Moody, S.; Gao, J. F.; Mai, Y. W. *In-situ* pull-off of ZnO nanowire from carbon fiber and improvement of interlaminar toughness of hierarchical ZnO nanowire/carbon fiber hydrid composite laminates. *Carbon* **2016**, *110*, 69–78.
[44] Li, M.; Zhang, S. B.; Li, L. W.; Han, J. Y.; Zhu, X. L.; Ge, Q. F.; Wang, H. Construction of highly active and selective polydopamine Modified hollow ZnO/Co_3O_4 p-n heterojunction catalyst for photocatalytic CO_2 reduction. *ACS Sustain. Chem. Eng.* **2020**, *8*, 11465–11476.
[45] Liang, Y. C.; Shao, H. C.; Liu, K. K.; Cao, Q.; Deng, Y.; Hu, Y. W.; Yang, K.; Jiang, L. Y.; Shan, C. X.; Kuang, L. M. et al. Visualizing motion trail via phosphorescence carbon nanodots-based delay display array. *ACS Appl. Mater. Interfaces* **2024**, *16*, 26643–26652.
[46] Jiang, L. Y.; Zhou, Y. C.; Zhang, S. F.; Shao, H. C.; Liang, Y. C. Time division colorful multiplexing based on carbon nanodots with modifiable colors and lifetimes. *Nano Lett.* **2024**, *24*, 8418–8426.
[47] Cao, Q.; Liu, K. K.; Liang, Y. C.; Song, S. Y.; Deng, Y.; Mao, X.; Wang, Y.; Zhao, W. B.; Lou, Q.; Shan, C. X. Brighten triplet excitons of carbon nanodots for multicolor phosphorescence films. *Nano Lett.* **2022**, *22*, 4097–4105.
[48] Li, K.; Skolrood, L. N.; Aytug, T.; Tekinalp, H.; Ozcan, S. Strong and tough cellulose nanofibrils composite films: Mechanism of synergetic effect of hydrogen bonds and ionic interactions. *ACS Sustain. Chem. Eng.* **2019**, *7*, 14341–14346.
[49] Fu, J. W.; Chen, Z. H.; Wang, M. H.; Liu, S. J.; Zhang, J. H.; Zhang, J. N.; Han, R. P.; Xu, Q. Adsorption of methylene blue by a high-efficiency adsorbent (polydopamine microspheres): Kinetics, isotherm, thermodynamics and mechanism analysis. *Chem. Eng. J.* **2015**, *259*, 53–61.
[50] Li, J.; Tan, L.; Liu, X. M.; Cui, Z. D.; Yang, X. J.; Yeung, K. W. K.;

Chu, P. K.; Wu, S. L. Balancing bacteria-osteoblast competition through selective physical puncture and biofunctionalization of ZnO/polydopamine/arginine-glycine-aspartic acid-cysteine nanorods. *ACS Nano* **2017**, *11*, 11250–11263.

[51] Liu, M.; Peng, Y.; Nie, Y. B.; Liu, P.; Hu, S.; Ding, J. S.; Zhou, W. H. Co-delivery of doxorubicin and DNAzyme using ZnO@polydopamine core–shell nanocomposites for chemo/gene/photothermal therapy. *Acta Biomater.* **2020**, *110*, 242–253.

[52] Ye, Q.; Zhou, F.; Liu, W. M. Bioinspired catecholic chemistry for surface modification. *Chem. Soc. Rev.* **2011**, *40*, 4244–4258.

[53] Zhao, W. B.; Liu, K. K.; Wang, Y.; Li, F. K.; Guo, R.; Song, S. Y.; Shan, C. X. Antibacterial carbon dots: Mechanisms, design, and applications. *Adv. Healthcare Mater.* **2023**, *12*, 2300324.

[54] Zhou, R.; Cui, D. J.; Zhao, Q.; Liu, K. K.; Zhao, W. B.; Liu, Q.; Ma, R. N.; Jiao, Z.; Dong, L.; Shan, C. X. Effective control of microbial spoilage in soybeans by water-soluble ZnO nanoparticles. *Food Chem.* **2022**, *388*, 132994.

[55] Liang, Y. C.; Shao, H. C.; Liu, K. K.; Cao, Q.; Jiang, L. Y.; Shan, C. X.; Kuang, L. M.; Jing, H. Thermally enhanced phosphorescent carbon nanodots for monitoring cold-chain logistics. *Small* **2024**, *20*, 2312218.

[56] Liang, Y. C.; Cao, Q.; Deng, Y.; Wang, Y.; Liu, K. K.; Shan, C. X. Triggering triplet excitons of carbon nanodots through nanospace domain confinement for multicolor phosphorescence in aqueous solution. *Nano Res.* **2024**, *17*, 6534–6543.

[57] Qin, J. X.; Yang, X. G.; Shen, C. L.; Chang, Y.; Deng, Y.; Zhang, Z. F.; Liu, H.; Lv, C. F.; Li, Y. Z.; Zhang, C. et al. Carbon nanodot-based humidity sensor for self-powered respiratory monitoring. *Nano Energy* **2022**, *101*, 107549.

[58] Chen, Y. X.; Xu, X. M.; Wang, Z. W.; Hua, G. Y.; Zhang, Y. H.; Liu, F. Q. Dehydration-modulated pomelo peel cellulose nanofiber interlayer customized polyamide membrane with highly uniform pores for efficient nanofiltration. *Chem. Eng. J.* **2024**, *496*, 154128.

[59] Guillen-Burrieza, E.; Servi, A.; Lalia, B. S.; Arafat, H. A. Membrane structure and surface morphology impact on the wetting of MD membranes. *J. Membr. Sci.* **2015**, *483*, 94–103.